A Novel Direct-Drive Rotary–Linear Machine and Ripple Reduction by Harmonic Current Injection Approach

Yue Ma, Shuangxia Niu, *Senior Member, IEEE*, Weinong Fu, and Jiaqi Fei

***Abstract*—This article presents a direct-drive multistage rotary–linear machine (RLM) with a dual permanent magnetic (PM) structure. The RLM has prominent direct-drive characteristics, such as high torque/force density, and a deeply integrated mechanical structure, as well as a significant degree of decoupling between the two dimensions of motion. A harmonic current injection method is proposed to reduce torque and force ripples, which are mainly caused by machining tolerances and manufacturing processes. The basic structure, winding design, and design deduction of the proposed RLM are introduced first. Then, the electromagnetic performance of the proposed dual-PM RLM is evaluated by finite element analysis and compared with the data of an existing RLM and the model with mechanical tolerance. Furthermore, the harmonic current injection (HI) method is designed. HI is adopted in motor control to effectively reduce the torque and force ripples of the machine and enhance the controllability of the RLM motor. Finally, the feasibility of the design scheme and HI is confirmed by testing the prototype.**

***Index Terms*—Current control, electromagnetic analysis, harmonic analysis, permanent magnet motors, PI control, torque measurement.**

I. Introduction

TWO-DEGREES-OF-FREEDOM (2-DoF) direct-drive machines can realize linear, rotary, and spiral motions without an intermediate transmission mechanism. Therefore, they can be widely used in various automation applications, such as numerical control machine tools, robots, automotive transmission devices, and other equipment, to upgrade performance. Nowadays, the 2-DoF function is usually achieved with two or more rotating motors and ball screw transmission devices. This structure has a complex control system, low reliability, and a high maintenance cost. Using one rotary–linear machine (RLM) instead of two or more rotating motors and transmission devices can significantly simplify the structure of the mechanical system, save space, and reduce weight, thus improving the accuracy and dynamic performance of the whole system, especially in robotic applications [1].

The RLM can exist in many forms. Some RLMs are partially helical in structure. The stator slots of the reluctance motor in [2] are helical-shaped. The stator excitation current has a combination of low-frequency and high-frequency components that excite force and torque, respectively. However, the high-frequency currents tend to introduce significant eddy current losses. In [3], [4], [5], and [6], the stator with three-phase helical windings excites a helical magnetic field, and the mover is driven by both axial force and circumferential torque at a fixed helical angle. The motor in [7] has an inner-layer helical permanent magnetic (PM) translator. When the outer stator generates a rotating magnetic field, the piecewise helical PM mover in the middle layer will move helically based on the magnetic fields of the inner and outer layers. However, a motor with a helical structure is challenging to produce, and it is difficult to decouple the torque and axial force of such motors.

A linear–rotary induction motor with two sets of windings was proposed in [8]. Two sets of orthogonal slots with separate three-phase windings are used to generate two magnetic fields, which provide rotary and linear movements [8], [9]. The mover in this motor can also adopt PM form and work in a synchronous motor state. However, such stator and winding designs are challenging for the actual application. Furthermore, although the motor in [8] achieves the decoupling of the two motion directions, the electromagnetic fields in the two directions will interfere with each other in the same space [10].

To address the problem of interference, the two-section stator structure is proposed in [11], [12], [13], [14], [15], and [16]. One section of the stator generates a rotating magnetic field, and the other provides a linear magnetic field. A 2-DoF induction motor whose stator is divided into two parts along the diameter is shown in [11] and [12]. Although the radial and axial magnetic field interference is weakened by applying such a structure, the originally closed phase-to-phase magnetic flux linkage is broken. Fluctuations of torque and force are increased as a result. At the same time, the two parts of the stator have different

Manuscript received 28 March 2023; revised 25 July 2023; accepted 22 August 2023. Date of publication 28 August 2023; date of current version 23 October 2023. This work was supported by the Research Grant Council of the Hong Kong Government under Project PolyU 152109/20E. Recommended for publication by Associate Editor J. Hur. *(Corresponding author: Shuangxia Niu.)*

Yue Ma and Shuangxia Niu are with the Department of Electrical and Electronic Engineering, The Hong Kong Polytechnic University, Kowloon, Hong Kong (e-mail: 17902301r@connect.polyu.hk; eesxniu@polyu.edu.hk).

Weinong Fu is with the Department of Computer Science and Control Engineering, Shenzhen Institutes of Advanced Technology Chinese Academy of Sciences, Shenzhen 518172, China (e-mail: wn.fu@siat.ac.cn).

Jiaqi Fei is with the Han's Robot, Han's Laser Smart Equipment Group, Company, Ltd., Shenzhen 518000, China (e-mail: jiaqifei0711@gmail.com).

Color versions of one or more figures in this article are available at https://doi.org/10.1109/TPEL.2023.3309378.

Digital Object Identifier 10.1109/TPEL.2023.3309378

magnitudes of attraction to the mover. Therefore, the pressure on the bearings is increased, which leads to an increase in friction. In [13], the core of the mover is a hollow cylinder. It has a surface-mounted Halbach PM array on the inner and outer surfaces. Both stator sections, distributed on the outer and inner sides of the mover, are used to promote the rotary and linear motions of the mover, respectively. The motor combines the characteristics of a brushless rotary motor and a voice coil linear motor. In order to improve the linear motion performance, in [17] and [18], the stator, which provides the axially varying magnetic field, is placed in the outer layer, and the outer layer of the mover adopts a multipole pair PM structure. With a sandwich-like structure, the machining and assembly processes of motors are strict. Different from the internal and external distribution of the two-section stator, the motors in [14], [15], and [16] are composed of two cylindrical stator sections arranged axially along the permanent magnet synchronous motor (PMSM). For this kind of motor, it is relatively simple to manufacture, and the magnetic fields in the two directions would hardly affect each other.

An induction motor arranged with four separate linear motor stators circumferentially is presented in [19]. By adjusting the phase sequence of the supply voltage between adjacent stators, the motor generates axial force and torque. Based on this design, the induction motor can also use four stators such as an ordinary rotary motor [20]. In addition, multiple independent stators can also be arranged axially and combined with the reluctance motor principle to design an RLM [21], [22], [23].

Based on the research of multiple separate stator sections, an RLM with multiple stator salient poles is proposed in [24], [25], and [26]. The stator core consists of regularly staggered salient poles fixed to an external yoke, and each salient pole has its own coil. Such windings are quite complicated. A similar stator structure was applied to the motor in [27] and [28]. Meanwhile, based on the principle of the surface-mounted PMSM, the PM distribution of the mover is arranged according to the position of the convex pole of the stator. Motor motion control is based on the magnetic field curvature factor calculated in the axial and circumferential directions [29], [30], [31]. It will increase the complexity of the control algorithm.

The machine with a combination of two motors along the axial direction has been widely used in the industry. This topology has advantages such as robustness and controllability, [1], [32], [33]. However, the linear motion stroke of the motors in this structure is short. It is only suitable for short-distance operations, such as gear transmission [33].

The RLM proposed in this article is an outer stator with an inner mover, and the two sections of the stator, which are arranged in the axial direction such as in [14], [15], and [16], are used to generate varying circumferential and axial magnetic fields. The overall machining is less difficult with this structure. The magnetic fields in both directions of the motor almost have no interference with each other. Compared to the motors in [24], [25], and [26], the control of the motor proposed in this study is easier. Most of the existing RLMs have low torque and force densities. Obvious torque and force ripples are insurmountable problems. This research focuses on the flux-modulation Vernier structure with dual-PM to improve torque and force densities. The flux-modulation structure has satisfied torque and the simple armature winding, which has been demonstrated in [34] and [35]. Better performances are achieved by dual-PM motors with lower magnetic resistance in the zone of relatively low current compared with traditional PMSM [36], [37], [38]. The novel dual-PM direct-drive RLM is proposed based on the magnetic field modulation principle. It has better controllability and higher output torque and force densities compared to other RLMs. The application of the modular linear stator avoids the force ripple introduced by the break of the magnetic flux linkage. The critical point of the RLM design is that the middle segment of the mover can coordinate with the stator to produce two-dimensional (2-D) motion. This allows the novel RLM to have a longer stroke compared to the motor in [33]. The application of the three-stage mover in this research enables torque and force at each position to be maximized. Due to the complicated process requirements of the Halbach PM array, the permanent magnet width of the proposed RLM is slightly smaller than the slot width, which reduces leakage and thus increases the air gap magnetic density. However, the novel RLM has a small magnetoresistance. Torque and force waveforms are sensitive to mechanical processing. This results in the measured torque and force ripples of the prototype being significantly larger than the simulation results. Therefore, whether the ripple problem can be solved is the key to determining the direct-drive performance of the proposed RLM.

Current optimization and harmonic information are the research focus points for ripple reduction in this article. Aiming at a steady rotation speed, in [39], [40], and [41], the method of performance compensation with the harmonic current has been adopted. This method also effectively compensates for the cogging torque and reduces the large torque fluctuations inherent in electromagnetic design [42], [43]. In this study, a harmonic injection (HI) method is proposed to solve the ripple problem.

The organizational structure of this article is as follows. Section II first introduces the RLM's basic structure, detail size, and design deduction. Section III presents the finite element analysis (FEA) results of RLM. It includes the distribution of magnetic fields, back electromotive force (back EMF), torque, and force. Here, the proposed RLM was compared directly with an existing PM RLM in other research. After that, the effect of mechanical tolerances on motor performance is analyzed by simulation. In Section IV, a method to reduce ripple is proposed. The effectiveness and robustness of HI are proven by theoretical explanations and simulation data. In Section V, the prototype is tested. This part mainly focuses on the output torque and axial force of the motor, respectively. The proposed ripple reduction approach was further tested for validity. Section VI presents the conclusion of this article.

II. Machine Structure

A. Fundamental Configuration

The whole structure of the dual-PM synchronous RLM adopts an internal mover and external stator. Fig. 1 depicts a 2-D illustration of the proposed RLM. The rotary motor in Fig. 1(a) and the linear motor in Fig. 1(b) are the foundations for the design

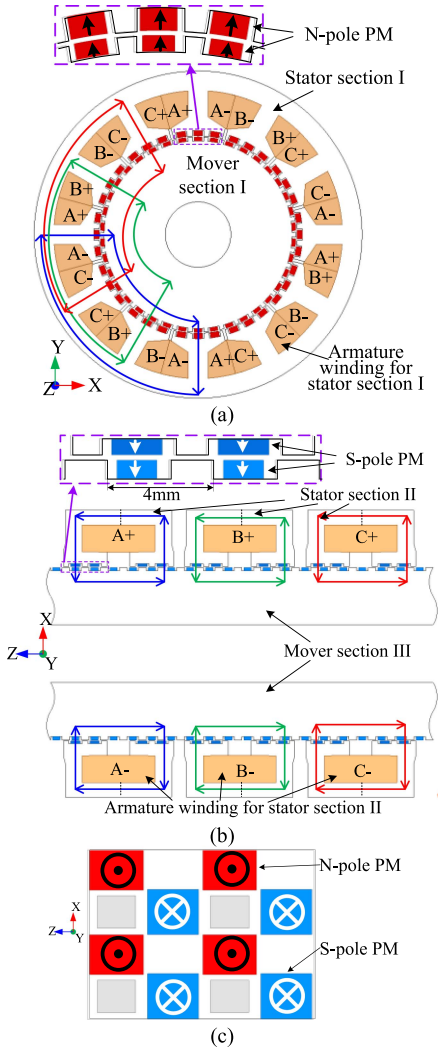

Fig. 1. 2-D illustration of the proposed RLM. (a) 2-D cross-sectional view of mover section I and stator section I coordination. (b) 2-D cross-sectional view of mover section III and stator section II coordination. (c) Partial planar expansion of mover section II.

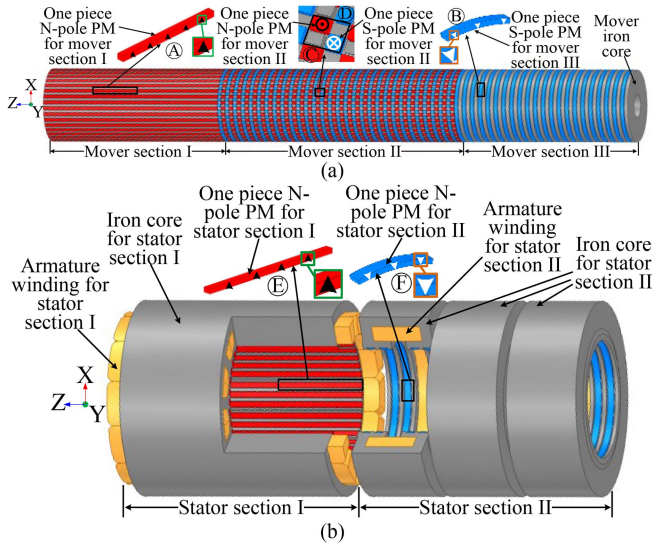

Fig. 2. Fundamental configuration of the proposed RLM. (a) Mover of RLM. (b) Stator of RLM.

of the proposed RLM. By combining the structural elements of the rotor in Fig. 1(a) and the mover in Fig. 1(b), the structure in Fig. 1(c) is created. The mover with the basic structure in Fig. 1(c) is able to complete rotational motion under the effect of the stator in Fig. 1(a), and it can also be coordinated with the stator in Fig. 1(b) to complete linear motion. According to differences in basic structure, the mover and the stator of the proposed RLM can be regarded as three sections and two sections, respectively. In Fig. 2, the motor's 3-D construction is displayed. As shown in Fig. 2(a), the mover is designed with three sections along the axial direction. Different shapes of slots are milled at different positions in one iron cylinder to form three types of tooth and slot structures. The two-section stator is shown in Fig. 2(b). Magnetic isolation is provided by the space between the two stator sections.

In Fig. 1(a), the stator Section I cooperates with the mover Section I. Due to the limited space, the concentrated winding with a smaller end length is selected. The armature winding adopts a 12-slot double-layer structure. At the beginning of the design, the torque values of the motor with different pole-pair numbers of each part were compared. When the proportion of magnetic modulation is too large, the width of the PM and the tooth is narrow, and there will be an apparent magnetic leakage phenomenon. Finally, the mover, stator, and winding pole-pair numbers are 38, 36, and 2. The PMs for mover Section I and stator Section I have the same polarity, which is north-pole (N-pole).

The 3-D model of mover Section I is seen in Fig. 2(a). With bar-shaped teeth and slots machined along the axial direction, mover Section I is inserted with bar PMs in the slots. This section is only for rotary movement. The PM in each slot is spliced with four pieces of N-pole PMs in the same dimension. Stator Section I with PMs, as seen in Fig. 2(b), is applied for rotary movement. Every stator salient pole has a split-tooth structure forming bar-shaped teeth and slots along the axial direction. Each bar-shaped PM inserted in the slot comprises two N-pole PMs with the same dimension.

The traditional linear motor can be regarded as an expansion of a circular motor [44]. In [17], the stator salient poles at both ends of the linear motor are no longer physically connected, so the magnetic flux is cut off. The force ripple is enlarged. In the proposed RLM, three stator modules were adopted in stator Section II [see Fig. 1(b)]. With a certain distance between adjacent modules, the magnetic isolation effect is created. Each modular iron core can be separated into two parts along a dotted line for simple wiring. In this way, the armature winding of each phase is wound into a ring coil and sandwiched between two parts. Because there is no end-winding, the proportion of copper loss is reduced, and the efficiency of energy conversion is increased. Each stator salient pole adopts three split teeth and two PMs. The south-pole (S-pole) PMs are adopted in stator Section II and mover Section III. In Fig. 1(b), the pole-pair pitch is 4 mm.

TABLE I
GENERAL DIMENSION PARAMETERS FOR PMS AND SLOTS

Symbol	Length	Arc angle	Inner radius	Width	Height	Slot width
A	22.0 mm			1.4 mm	0.7 mm	2.1 mm
B		30°	17.2 mm	1.5 mm	0.7 mm	2.4 mm
C	1.8 mm			1.6 mm	0.7 mm	2.0 mm
D	1.9 mm			1.4 mm	0.7 mm	2.25 mm
E	32.0 mm			1.6 mm	1.0 mm	2.05 mm
F		30°	18.1 mm	1.9 mm	0.6 mm	2.8 mm

TABLE II
DIMENSIONAL INFORMATION OF THE PROPOSED RLM

Items	Value
Stroke	120 mm
Outer diameter of the stator	60 mm
Air gap height	0.2 mm
Outer diameter of the mover	35.8 mm
Inner diameter of the stator	36.2 mm
Effective axis length of SFRM	64 mm
Effective axis length of SFLM	74 mm
Total length of the stator	150 mm
Turns of stator section I	41
Turns of stator section II	87

As seen in Fig. 2(a), mover Section III has annular teeth and annular PMs in the slots. This section is just dedicated to linear movement. The annular PM in each slot comprises 12 pieces of S-pole arc-shaped PMs with the same dimension. The shape of the iron core for stator Section II in Fig. 2(b) is similar to a hollow ring. A ring-shaped armature winding is installed inside the iron core. Each iron core module holds two stator salient poles whose surfaces have a structure of divided teeth and slots. Every slot is filled by an arc-shaped S-pole annular PM made up of 12 identically sized pieces.

In Figs. 1(c) and 2(a), mover Section II is composed of square teeth and square PMs, which have two different polarities in the slots, and this section is designed for both rotary and linear movement. Both teeth and PMs are small. The relative positions of PMs, teeth, and slots can be visualized in Fig. 1(c). In the circumferential direction of the motor, the slots adjacent to the teeth are inserted with N-pole PMs, and in the axial direction of the motor, the slots adjacent to the teeth are inserted with S-pole PMs. In order to ensure the performance linkage with mover Sections I and III, the 38 pole pairs in the circumferential direction and the 4 mm pole pair pitch in the axial direction are required. Mover Section II is the major point of the motor design. It will be described in detail later.

As shown in Figs. 1 and 2, the N-pole PM indicates that the flux direction of the PM is outward in the radial direction, and the S-pole PM has the opposite flux direction to the N-pole PM. To reduce the flux leakage of the PM, the slot width is larger than the PM width. The PM is located in the middle of the slot. This structure is easier to manufacture than the Halbach PM, and it improves the air gap magnetic density just slightly less than the Halbach PM structure. The results of each PM size and corresponding slot width after dimension optimization with a multiobjective genetic algorithm are given in Table I. Compared with only rotor PMs or only stator PMs excitation, the structure of the dual-PM modulation can significantly improve the density of torque and force of the motor [36], [38].

The standard stroke of the prototype is 120 mm. The outer diameter of the motor stator is 60 mm, the outer diameter of the mover is 35.8 mm, and the air gap height is 0.2 mm. The effective shaft lengths of the two sections of the stator are 64 mm and 74 mm, respectively. Calculating the length of the end-winding, the total length of the stator is 150 mm. The above dimensional information is summarized in Table II. In the whole stroke of the RLM, stator Section I will interact with mover Sections I and II to generate rotation torque. Axial force will be produced by the interaction of the mover parts II and III with the stator Section II. The rotary and linear movements are controlled separately by two sets of armature windings. Sections I and II of the stator have 41 and 87 winding turns, respectively. With the proposed RLM, 2-DoF can be freely combined or completely decoupled.

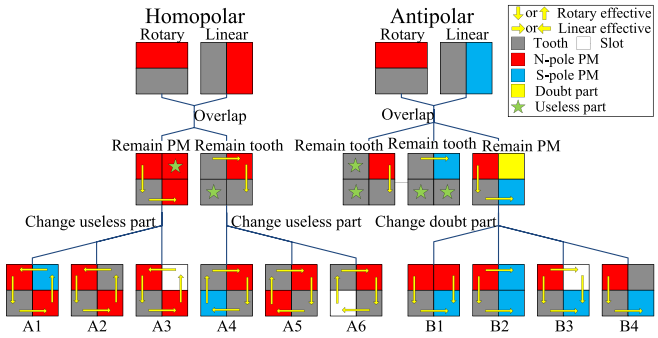

Fig. 3. Deduction of PM polarities for the RLM.

B. Mover Design and PM Polarities

The whole motor design is focused on mover Section II. This section should ensure that it not only cooperates with the stator Section I to produce torque and rotary movement but also cooperates with the stator Section II to produce force and linear movement. At the same time, to maintain higher torque and force production, the mover Section II is designed with a tooth-PM structure.

At the beginning of the design, it was determined that the proposed RLM would adopt the dual-PM structure in Fig. 1(a) and (b) as the basis for the entire stator and mover Sections I and III. The mover Section II and PM polarity for each part of the RLM are derived in Fig. 3. The overall approach is to overlap the valid structures of mover Sections I and III. After retaining the common part, one of the different structures in the overlapping section is selectively retained. The validity of the new structure in both directions of movement is evaluated again. Finally, the invalid or doubtful parts are replaced by the new structure, and then the validity of the final structure for both directions of motion is analyzed.

As a dual-PM flux-modulation Vernier motor, the RLM has to follow both the principle of a PMSM and the characteristics of the reluctance motor [45]. Therefore, for the structure selection

of the mover, the relationship between reluctance and magnetic flux density with position should be considered. Additionally, mean torque and mean force are related to the fundamental harmonic values of reluctance and magnetic flux density. Thus, the new structure in the same direction of motion is required to have almost the same fundamental phase angles of magnetic flux density and relative magnetic permeability as the original effective structure, respectively. This is the precondition for being selected as the basic structure of mover Section II.

When PMs in mover Sections I and III are homopolar, the inference process is shown on the left half of Fig. 3. Here, the N-pole PM is utilized as an illustration. The S-pole PM has the same impact as the N-pole PM. For tooth and PM overlapping, one part is invalid, whichever element is retained. By replacing the invalid part, six structures from A1 to A6 are produced. When PMs in mover Sections I and III are antipolar, the inference process is shown in the right half of Fig. 3. After the overlap procedure, there are generally three cases, as shown in Fig. 3. The first two structures can only effectively create motion in one direction since they have two worthless sections. The last one has two PMs of different polarities overlapping in the upper right corner. This part is temporarily regarded as a doubt part. After replacing the doubtful part with different elements, the four structures B1–B4 are created.

Taking the analysis of B3 validity as an example, it is shown in Fig. 4. The basic unit in B3 is divided into four effective structures along two mutually vertical directions of motion, as shown in Fig. 4(a). The magnetic field of these four structures is analyzed in 2-D. By analyzing the magnetic flux density and relative permeability for four positions, which are R1-R1', R2-R2', L1-L1', and L2-L2', the results in Fig. 4(b) can be obtained. The fundamental components of magnetic flux density B_1 and relative permeability μ_1 are shown in Fig. 4(b). It can be shown that regardless of the direction of rotation or linear motion, the phase angle of the fundamental harmonic of magnetic flux density is the same for the two structures in the same direction. Furthermore, the fundamental harmonic of relative permeability has the same phase angle. According to the previous study, it can be concluded that the rotating magnetic field generated by the stator in Fig. 1(a) can drive the mover, which is composed of R1-R1' and R2-R2', to rotate. Similarly, the stator in Fig. 1(b) provides an axial magnetic field that can lead the mover composed of L1-L1' and L2-L2' to move linearly.

However, in A1 to A6, for the five structures except A4, the fundamental harmonic phase angles of magnetic flux density are almost opposite for the two effective structures in each direction of motion. Although the fundamental harmonic phase angle of magnetic flux density is almost the same in A4, the phase angle of the relative permeability fundamental harmonic is totally opposite. Therefore, when coupled to the same stator structure, the two effective sections will simultaneously produce two torques or forces that are directed in opposing directions.

Considering that the motion effect of the whole motor is relatively balanced in the two motion directions, the structure of B3 is adopted in mover Section II. The 3-D form is shown in Fig. 2(a). The polarity direction of the PMs in the other four sections is determined after the structure of mover Section II is settled. The whole proposed RLM is confirmed as the model in Fig. 2.

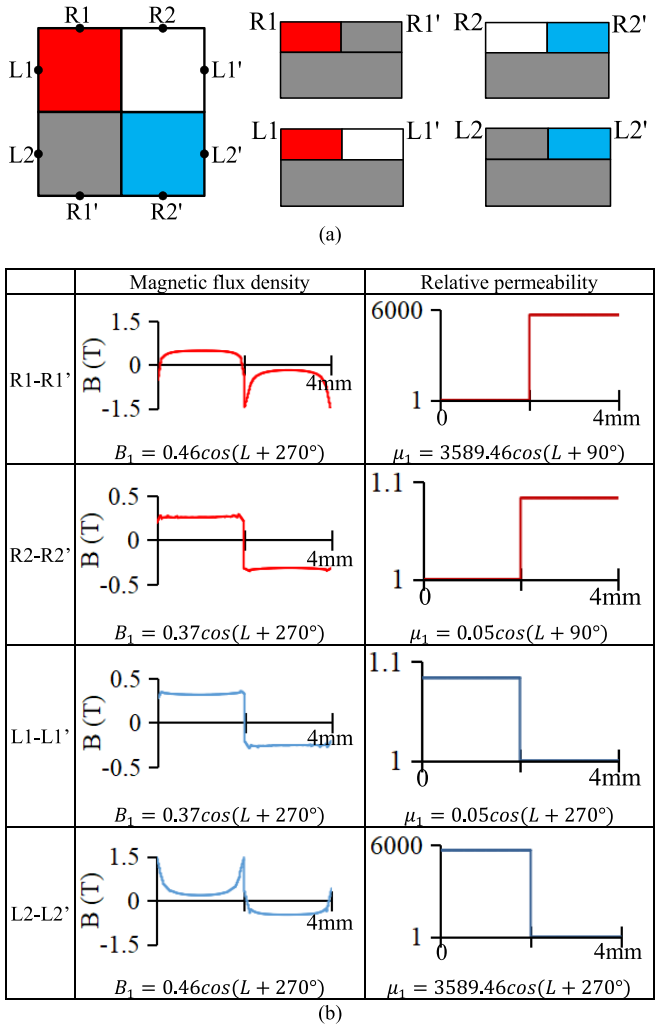

Fig. 4. Effectiveness analysis of B3. (a) Four effective structures of B3. (b) Magnetic flux density and relative permeability analysis.

III. Electromagnetic Performance Analysis

A. Magnetic Field Distribution

The distribution of magnetic flux and magnetic field intensity with rated current excitation at rated speed is shown in Figs. 5 and 6. The rotation and linear structures are symmetrical. When the magnetic field distribution is shown in the figure, one-half shows the flux distribution, and the other half shows the magnetic field intensity distribution. Fig. 5(a) corresponds to the magnetic field distribution in the cross section of the mover with N-pole PM and tooth structure for rotary movement. The magnetic field distribution in the cross section of the mover with S-pole PM and slot is shown in Fig. 5(b). The two-pole magnetic fields excited by the armature winding are visible in one half of the figure. The overall magnetic field intensity in Fig. 5(a) is higher than in Fig. 5(b). Higher flux density leads to higher torque, but in

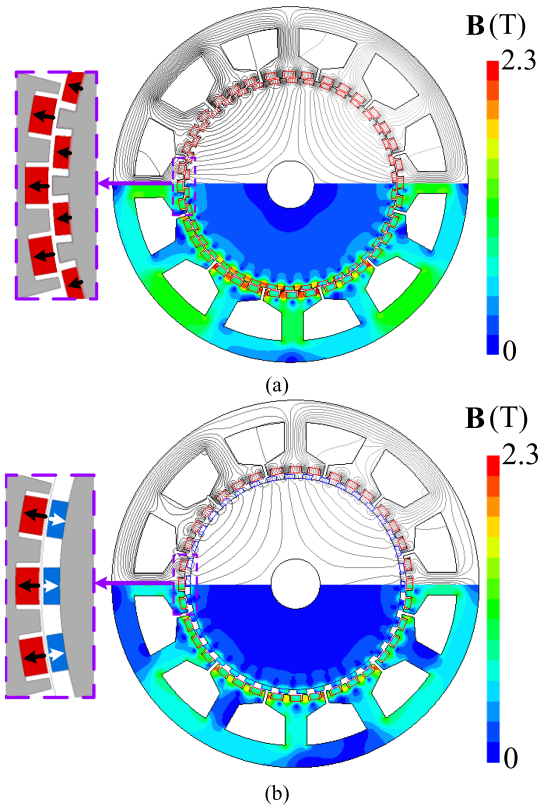

Fig. 5. Magnetic field distribution of rotary movement structures. (a) Mover with tooth-PM structure. (b) Mover with slot-PM structure.

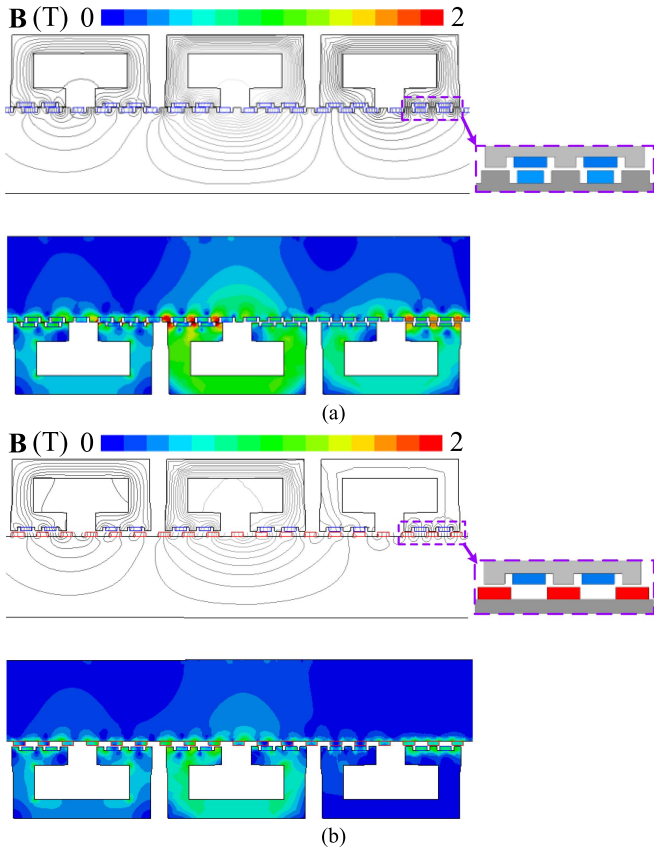

Fig. 6. Magnetic field distribution of linear movement structures. (a) Mover with tooth-PM structure. (b) Mover with slot-PM structure.

order to ensure rotational and linear motions, both structures in Fig. 5 are necessary for mover Section II at the same time.

Fig. 6(a) and (b) shows the structure of the motor for linear movement. From the flux distribution of both figures, it can be seen that when the stator of the linear motion is modular, the stator yoke is only connected with the two stator salient poles related to the same phase winding. This structure increases the reluctance between the different stator phases. The flux excited by each phase winding will form a closed loop in a module. It is rarely affected by flux from other modules. In this way, a flux loop will hardly form between the stator modules of other phases. This structure can effectively reduce force fluctuation. The structure of the mover in Fig. 6(a) is S-pole PM and teeth, and it is a slot and N-pole PM structure shown in Fig. 6(b). The magnetic field intensity in split teeth is higher than in normal structures. Furthermore, the overall magnetic field intensity of the linear part is lower than that of the rotating part. It means that the rated state of the linear part is farther away from the state of magnetic saturation. Therefore, when the load current is higher than the rated value, the performance of the linear part will be slightly better than that of the rotary part.

B. Torque and Force FEA

The following four states of the motor are mainly studied. When the mover Section I is within the effective electromagnetic range of the stator Section I, the mover's rotating motion is named rotary movement state I. When the mover Section II is within the effective electromagnetic range of stator Section I, the mover's rotary motion state is named rotary movement state II. When mover Section III is within the effective electromagnetic range of stator Section II, the mover's linear movement is named linear movement state I. When the mover Section II is within the effective electromagnetic range of the stator Section II, the mover's linear movement is named linear movement state II.

FEA is applied to study the performance of the RLM. The proposed RLM-rated load current of the two rotary movement states is 4 A, and the rated speed is 120 r/min. When the RLM is in rotary movement state I, the no-load back EMF is shown in Fig. 7(a). The fundamental wave amplitude is 10.73 V. The torque of an electrical period at a stable speed is shown in Fig. 7(b). The average rated torque is 4.80 N·m, and the peak-to-peak (pk2pk) value is 0.20 N·m. When the RLM is in a rotary movement state II, the no-load back EMF and torque information of a steady-state electrical cycle are shown in Fig. 7(c) and (d). The fundamental wave amplitude of no-load back EMF is 6.75 V, and the mean torque and pk2pk values are 3.20 N·m and 0.17 N·m, respectively. In Fig. 7(b) and (d), it is evident that the sixth harmonic component of the torque ripple is prominent. The average torque of rotary movement state II was about 66.67% of the average torque of rotary movement state I.

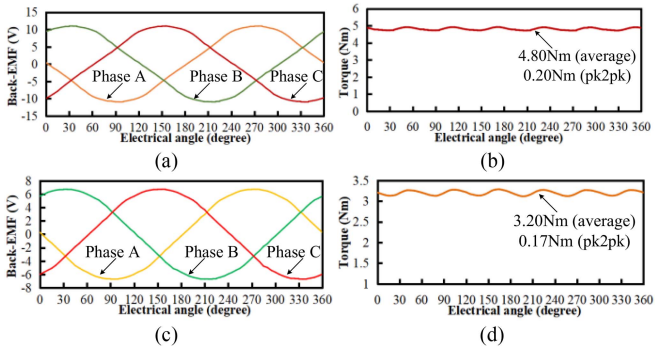

Fig. 7. FEA of rotary movement. (a) Back EMF for state I. (b) Torque waveform for state I. (c) Back EMF for state II. (d) Torque waveform for state II.

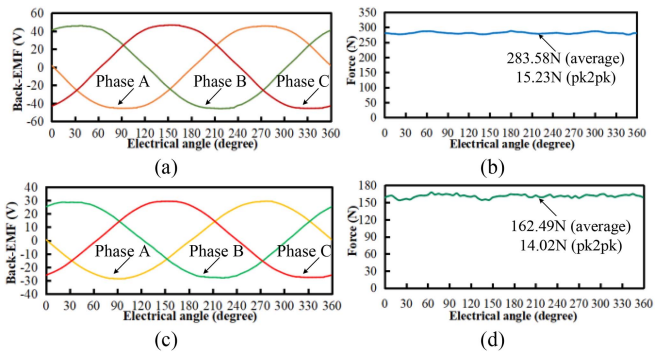

Fig. 8. FEA of linear movement. (a) Back EMF for state I. (b) Force waveform for state I. (c) Back EMF for state II. (d) Force waveform for state II.

The rated load current of the two linear movement states of RLM is 4 A, and the rated speed is 1 m/s. The no-load back EMFs in two linear motion states are shown in Fig. 8(a) and (c). The fundamental amplitudes were 47.49 V and 29.03 V, respectively. As shown in Fig. 8(b) and (d), the average force values at the rated current are 283.58 and 162.49 N. The ripple pk2pk values are 15.23 and 14.02 N. The average force of linear movement state II is about 57.30% of the value of linear movement state I.

C. Machine Comparative Study

An RLM with a Halbach PM array structure is introduced in [46]. To increase the force and torque, as shown in Fig. 9, the ironless stator in [46] is converted to an iron core stator, referring to [20]. It is used as a comparison motor. The torque and force at the same current load are compared with the data in Figs. 7(d) and 8(d). The stator's outer diameter is 100 mm. After adjusting the air gap height to 0.2 mm as well, the stator inner diameter is 38.4 mm and the mover outer diameter is 38 mm. These dimensions are similar to the proposed RLM. However, the effective axial length of the stator of the comparison motor is 75 mm.

The mean torque of the comparison motor was 1.09 N·m while maintaining the same current load as the proposed RLM. Since the effective axial length of the proposed RLM is 150 mm, which is twice as long as the comparison motor, the torque value of the

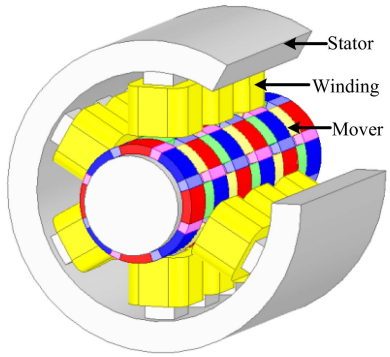

Fig. 9. Comparison RLM.

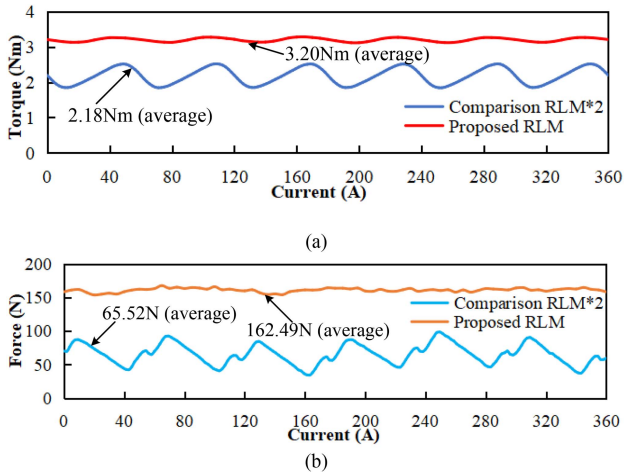

Fig. 10. Comparison of torque and force. (a) Torque comparison. (b) Force comparison.

comparison motor was expanded to twice the original value. The expanded value is 2.18 N·m, which is then compared with the proposed LRM's rated minimum mean torque of 3.20 N·m at the same axial length, as shown in Fig. 10(a). Similarly, the mean force of the comparison motor is 32.76 N. After doubling the value, it is 65.52 N. Fig. 10(b) shows a comparison with the rated minimum mean force of 162.49 N for the proposed LRM. It is apparent that while having approximately the same volume, the proposed RLM has a significantly larger force and torque than the comparison RLM. Additionally, the force and torque fluctuations of the former are significantly smaller than those of the latter.

The mover of the comparison motor is nearly completely covered by PMs, whose thickness is 3 mm. However, only about half of the mover's surface is covered by PMs in the proposed RLM, and the thickness of the PM is no more than 1 mm. Even if PMs are also placed in the proposed stator slots, the total volume of PMs used in the proposed RLM is less than half of the PMs used in the comparison motor. This ratio will decrease as the stroke increases. Compared to the Halbach magnetic array, PM insertion in the proposed RLM is not as difficult as the process of the Halbach PM array, but it is quite time consuming. In practice, the slot is slightly deeper at the PM inset point in order

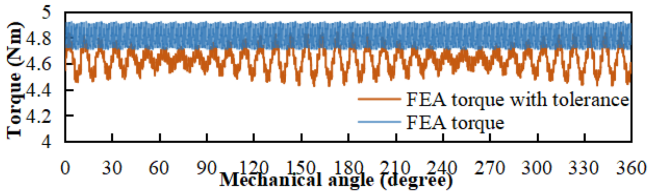

Fig. 11. Torque waveforms comparison.

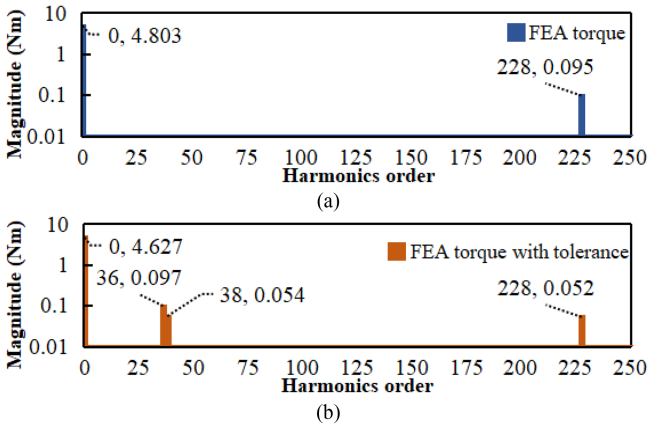

Fig. 12. Frequency spectrum analysis. (a) Original model. (b) Model with tolerance.

to locate the PM inset. In a Halbach PM array, PMs oriented in different directions will repel each other. However, in the proposed RLM, each slot with only one polarity PM is more stable.

D. Simulation With Tolerance

Above is the simulation analysis for the perfect model. There must be tolerances in the actual machining. Because the standard value of the air gap between the stator and mover is only 0.2 mm, the performance of the motor is easily affected by the difference in machining size. For example, the PMs inserted in the slot have a small volume, especially the square PMs in the middle section. Tiny tolerance values may produce more significant magnetic energy differences. The machining size of both stator and mover cores is set with tolerances as well. These factors will cause torque and force fluctuations to increase. In order to confirm this idea, the simulation analysis of the model with tolerances is presented as follows.

In the mechanical drawing of the core parts, the machining tolerance of the mover outer radius and stator inner radius is ± 0.03 mm, and the runout is 0.04 mm. Now, the previous tolerance information is randomly applied to the modeling of the combination in Fig. 1(a), and then the simulation of the new model is performed. The new torque waveform is compared with the torque waveform of the standard model in Fig. 11. These two waveforms are obviously different, and the pk2pk value increases from 0.20 to 0.41 N·m. Frequency spectrum analysis of the two waveforms is performed using the fast Fourier transform (FFT), and the results are shown in Fig. 12. After adding the tolerance, the mean torque value and the fluctuation amplitude at the 228th frequency decrease slightly, while the fluctuation amplitude at the 36th and 38th frequencies increase significantly. This proves that the mechanical tolerances affect the torque fluctuations. However, the machining of each component in the prototype inevitably has tolerances. This can significantly increase the actual fluctuation values. The problem can be considered solved from the control aspect.

IV. Ripple Reduction

A. Harmonic Injection

In order to reduce the large torque ripple and force ripple of the prototype with mechanical tolerance, the HI algorithm is used to diminish the fluctuation. The advantage of this method is that the torque/force fluctuation due to all factors, including cogging torque/force and friction torque/force, can be reduced together.

Take the rotary state as an example. The spectrum analysis of the measured torque information by FFT in the position domain is obtained in the following form:

$$T = T_{\text{avg}} + \sum_{k=1}^{n} T_k \cos\left(k\theta_m + \varphi_k\right) \tag{1}$$

where T is the electromagnetic torque. T_{avg} is the average torque with an ordinary sinusoidal load current. k represents the harmonic order, and it is an integer greater than or equal to 1. T_k is the amplitude of the kth harmonic torque. φ_k is the phase angle of the kth harmonic torque. θ_m is the mechanical angle of rotation of the rotor. If the harmonic component $T_k\cos(k\theta_m + \varphi_k)$ intends to be eliminated, $T_k\cos(k\theta_m + \varphi_k + 180^\circ)$ should be used to superpose with the former. When the rotor rotates at a constant speed, according to the principle of equal electromagnetic power, there is

$$\omega_m T = P_e = IE\cos\varphi = I\,E_0 = I_a E_a + I_b E_b + I_c E_c \tag{2}$$

where ω_m is the rotor's mechanical angular velocity. P_e is electromagnetic power. I is the armature current. E is the air-gap EMF. φ is the angle between the air-gap EMF and the armature current. E_0 is the excitation EMF. Then the armature current and excitation EMF are written in the three-phase form. I_a, I_b, and I_c are the three-phase sinusoidal armature currents, which are the load current generating the mean torque. E_a, E_b, and E_c are the three-phase excitation EMF. The three-phase excitation EMF is written as a superposition of fundamental and harmonic waves as follows:

$$\begin{cases} E_a = \sum\limits_{k=1}^{n} E_k \cos\left(k\theta_m + \varphi_{uk}\right) \\ E_b = \sum\limits_{k=1}^{n} E_k \cos\left(k\theta_m + \varphi_{uk} - 120^\circ\right) \\ E_c = \sum\limits_{k=1}^{n} E_k \cos\left(k\theta_m + \varphi_{uk} + 120^\circ\right) \end{cases} \tag{3}$$

where E_k is the amplitude of excitation EMF harmonics. φ_{uk} is the harmonic phase angle of excitation EMF. The component associated with the mean torque value generated by the load

current is the dominant of the excitation EMF as follows:

$$\begin{cases} E_{a1} = E_{pn}\cos\left(p_n\theta_m + \varphi_{upn}\right) \\ E_{b1} = E_{pn}\cos\left(p_n\theta_m + \varphi_{upn} - 120^\circ\right) \\ E_{c1} = E_{pn}\cos\left(p_n\theta_m + \varphi_{upn} + 120^\circ\right) \end{cases} \tag{4}$$

that is the dominant of the excitation EMF when k is equal to p_n. Here, p_n is the rotor pole-pair number. If $T_k\cos(k\theta_m + \varphi_k + 180^\circ)$ wants to be obtained, the following will be built as:

$$\omega_m T_k\cos\left(k\theta_m + \varphi_k + 180^\circ\right) = I_{ak}E_{a1} + I_{bk}E_{b1} + I_{ck}E_{c1} \tag{5}$$

where I_{ak}, I_{bk}, and I_{ck} are the injected harmonic currents that are required to eliminate the kth harmonic torque, here

$$\begin{cases} I_{ak} = I_{mk}\cos\left(n_{ik}\theta_m + \varphi_{ik}\right) \\ I_{bk} = I_{mk}\cos\left(n_{ik}\theta_m + \varphi_{ik} - 120^\circ\right) \\ I_{ck} = I_{mk}\cos\left(n_{ik}\theta_m + \varphi_{ik} + 120^\circ\right) \end{cases}. \tag{6}$$

I_{mk} is the desired phase current amplitude. n_{ik} is the harmonic order of the desired phase current, and φ_{ik} is the desired phase current angle. When the amplitude of the injected harmonic current is small, the torque harmonics generated by the harmonic current interacting with other harmonics of the excitation EMF except for the fundamental part can be ignored. Substituting the harmonic current and the fundamental excitation EMF into (5), can obtain

$$\begin{aligned} &\omega_m T_k\cos\left(k\theta_m + \varphi_k + 180^\circ\right) \\ &= I_{mk}E_{pn}\cos\left(n_{ik}\theta_m + \varphi_{ik}\right)\cos\left(p_n\theta_m + \varphi_{upn}\right) \\ &\quad + I_{mk}E_{pn}\cos\left(n_{ik}\theta_m + \varphi_{ik} - 120^\circ\right) \\ &\quad \times \cos\left(p_n\theta_m + \varphi_{upn} - 120^\circ\right) \\ &\quad + I_{mk}E_{pn}\cos\left(n_{ik}\theta_m + \varphi_{ik} + 120^\circ\right) \\ &\quad \times \cos\left(p_n\theta_m + \varphi_{upn} + 120^\circ\right). \end{aligned} \tag{7}$$

Due to

$$\cos\alpha\cos\beta = \frac{1}{2}\left[\cos\left(\alpha+\beta\right) + \cos\left(\alpha-\beta\right)\right] \tag{8}$$

(7) can be rewritten as

$$\begin{aligned} &\omega_m T_k\cos\left(k\theta_m + \varphi_k + 180^\circ\right) \\ &= \frac{1}{2}I_{mk}E_{pn}[\cos\left(n_{ik}\theta_m + \varphi_{ik} + p_n\theta_m + \varphi_{upn}\right) \\ &\quad + \cos\left(n_{ik}\theta_m + \varphi_{ik} - 120^\circ + p_n\theta_m + \varphi_{upn} - 120^\circ\right) \\ &\quad + \cos\left(n_{ik}\theta_m + \varphi_{ik} + 120^\circ + p_n\theta_m + \varphi_{upn} + 120^\circ\right) \\ &\quad + \cos\left(n_{ik}\theta_m + \varphi_{ik} - p_n\theta_m - \varphi_{upn}\right) \\ &\quad + \cos\left(n_{ik}\theta_m + \varphi_{ik} - 120^\circ - p_n\theta_m - \varphi_{upn} + 120^\circ\right) \\ &\quad + cos\left(n_{ik}\theta_m + \varphi_{ik} + 120^\circ - p_n\theta_m - \varphi_{upn} - 120^\circ\right)] \\ &= \frac{3}{2}I_{mk}E_{pn}\cos\left(n_{ik}\theta_m + \varphi_{ik} - p_n\theta_m - \varphi_{upn}\right). \end{aligned} \tag{9}$$

And then, the following can be obtained:

$$\begin{aligned} &T_k\cos\left(k\theta_m + \varphi_k + 180^\circ\right) \\ &= \frac{3I_{mk}E_{pn}}{2\omega_m}\cos\left[\left(n_{ik} - p_n\right)\theta_m + \left(\varphi_{ik} - \varphi_{upn}\right)\right]. \end{aligned} \tag{10}$$

Therefore

$$T_k = \frac{3I_{mk}E_{pn}}{2\omega_m},\ k = n_{ik} - p_n,\ \varphi_k = \varphi_{ik} - \varphi_{upn} - 180^\circ \tag{11}$$

where T_k, k, and φ_k can be obtained by FFT analysis. Also, due to

$$\begin{cases} T_{\text{avg}} = \frac{3I_m E_{pn}}{2\omega_m} \\ T_k = \frac{3I_{mk}E_{pn}}{2\omega_m} \end{cases}. \tag{12}$$

Here, I_m is the sinusoidal load current amplitude for the average torque generation. When I_m is not equal to 0, the following can be calculated out as:

$$I_{mk} = I_m\frac{T_k}{T_{\text{avg}}},\quad n_{ik} = k + p_n,\quad \varphi_{ik} = \varphi_k + \varphi_{upn} + 180^\circ. \tag{13}$$

In this situation, T_{avg} is also not equal to 0, and this method can calculate I_{mk} more accurately because the excitation EMF during motor load operation cannot be measured directly, and the load current will distort the excitation EMF due to the magnetic saturation phenomenon of magnetic materials. It is also not necessary to measure the excitation EMF. So, when the load current is not 0, the harmonic component of torque $T_k\cos(k\theta_m + \varphi_k)$ needs to be eliminated, and harmonic currents need to be injected into the three-phase current, as follows:

$$\begin{cases} I_{ak} = I_m\frac{T_k}{T_{\text{avg}}}\cos\left[\left(k + p_n\right)\theta_m + \left(\varphi_k + \varphi_{upn} + 180^\circ\right)\right] \\ I_{bk} = I_m\frac{T_k}{T_{\text{avg}}}\cos\left[\left(k+p_n\right)\theta_m + \left(\varphi_k+\varphi_{upn}+180^\circ\right) - 120^\circ\right] \\ I_{ck} = I_m\frac{T_k}{T_{\text{avg}}}\cos\left[\left(k+p_n\right)\theta_m + \left(\varphi_k+\varphi_{upn}+180^\circ\right) + 120^\circ\right] \end{cases}. \tag{14}$$

On the other hand, when I_m is equal to 0, E_{m1} is the fundamental component of the no-load excitation EMF that can be measured directly. Thus

$$I_{mk} = \frac{2\omega_m T_k}{3E_{pn}}. \tag{15}$$

The linear movement of the motor can also be used in the same way to reduce force ripple. Because the amplitude of the harmonic current used to reduce the fluctuation is relatively small, the effect on the magnetic saturation and introduced fluctuations of the motor is almost negligible. This method reduces the ripple of torque and force while keeping the mean value unchanged. It makes the motor more controllable and improves the accuracy of the direct-drive motor.

B. Robustness Boundary

The method discussed above is to completely eliminate the harmonics of the corresponding frequencies, but in actual application, certain errors will exist due to reasons such as nonlinearity of materials, insufficient measurement accuracy, and signal delay. Therefore, the proposed method necessitates strong robustness. For the amplitude and phase angle involved in HI, the accuracy of amplitude measurement and calculation can be easily guaranteed. However, phase angle values are prone to

TABLE III
TORQUE FFT RESULTS AND CURRENT DATA OF HI FOR MODEL WITH MECHANICAL TOLERANCE

Case	k	T_k(Nm)	φ_k(°)	I_{mk}(A)	n_{ik}	φ_{ik}(°)
Model with	36	0.097	234.76	0.084	74	144.76
mechanical	38	0.054	268.95	0.047	76	178.95
tolerance	228	0.052	39.76	0.045	266	309.76

errors, especially in the case of high-frequency harmonics, due to aspects such as transmission delays and a lack of measurement accuracy. In the following, the phase angle range in which fluctuations can be reduced is investigated based on the accurate amplitude of harmonic currents.

$$\begin{aligned}&\omega_m T_k \cos\left(k\theta_m+\varphi_k\right)\\&\quad+\omega_m T_k \cos\left(k\theta_m+\varphi_k+\Delta\varphi+180^\circ\right)\\&=2\omega_m T_k \cos\frac{2k\theta_m+2\varphi_k+\Delta\varphi+180^\circ}{2}\cos\frac{-\Delta\varphi-180^\circ}{2}\\&=2\omega_m T_k \cos\frac{\Delta\varphi+180^\circ}{2}\cos\left(k\theta_m+\varphi_k+\frac{\Delta\varphi}{2}+90^\circ\right).\end{aligned}\tag{16}$$

Here, $\Delta\varphi$ represents the error of phase angle. When the amplitude of (16) is less or equal to the amplitude of the original harmonic, it means that the harmonic amplitude is reduced. Therefore, when

$$\left|2\omega_m T_k \cos\frac{\Delta\varphi+180^\circ}{2}\right|\le\omega_m T_k \tag{17}$$

$$\left|\cos\frac{\Delta\varphi}{2}+90^\circ\right|\le\frac{1}{2} \tag{18}$$

$$-\frac{1}{2}\le\sin\frac{\Delta\varphi}{2}\le\frac{1}{2} \tag{19}$$

it can be concluded that

$$-60^\circ\le\Delta\varphi\le60^\circ. \tag{20}$$

According to (13), the phase angle error range of the input current should also be as shown in (20). Thus, as long as the error of phase angle is within the range of $\pm60^\circ$, it will still have the effect of reducing the corresponding frequency torque harmonics. This range of effective phase angle is large, and it is difficult to make the error of phase angle larger than this effective range under correct operation.

C. Simulation Verification

The data for the 36th, 38th, and 228th torque harmonics in Fig. 12(b) and the current data used to eliminate these harmonics are given in Table III. Here, the fundamental phase angle φ_{upn} is 90° and I_m is equal to 4 A. The mean torque in Fig. 12(b) is 4.627 N·m. Then, the harmonic current data is substituted into (14) to obtain the new three-phase currents, which are then fed into the simulation model with mechanical tolerances. The A-phase current waveform is shown in Fig. 13. This waveform is slightly different from the regular sinusoidal current waveform due to HI. Under the effect of harmonic current, the torque

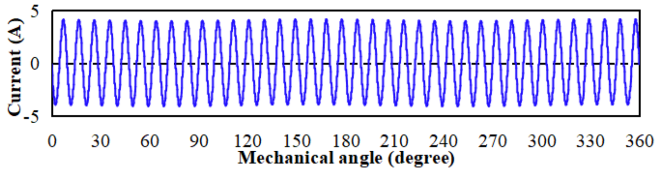

Fig. 13. A-phase current with HI.

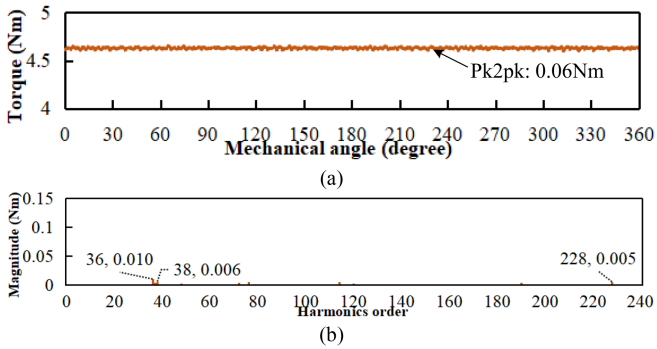

Fig. 14. Simulation of the torque ripple reduction with HI. (a) Torque waveform. (b) FFT result.

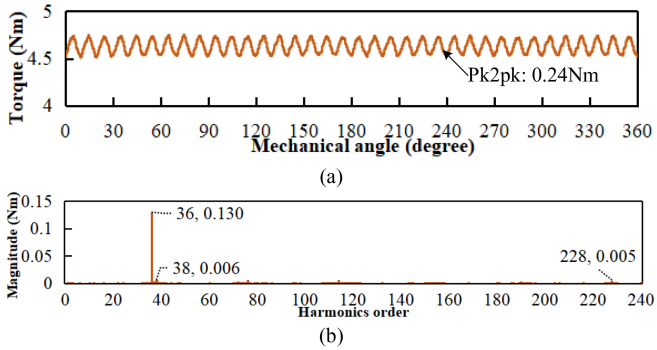

Fig. 15. HI Robustness verification. (a) Torque waveform of simulation. (b) FFT result.

waveform is shown in Fig. 14(a). It can be seen that the ripple is significantly reduced compared to Fig. 11. In this case, the value of torque pk2pk is only 0.06 N·m. The frequency analysis of the torque ripple by removing the mean torque is provided in Fig. 14(b). In the simulation result, the 36th, 38th, and 228th torque harmonics are almost completely eliminated.

If there is a certain error in the phase angle of the harmonic current, for example, when the φ_{i36} is changed to 234.76° at this time with the other data in Table III unchanged, that means the deviation angle of the φ_{i36} reaches the 90°. According to the calculation of the robustness boundary, this has exceeded the boundary of the effective phase angle. Here, the prediction is that it will cause an increase in the amplitude of the 36th harmonic, but the 38th and 288th frequencies will still be eliminated. In this case, the simulation with the mechanical tolerance model is carried out to obtain Fig. 15(a), and a frequency spectrum analysis of Fig. 15(a) is presented in (b). The value of the torque fluctuation pk2pk is 0.24 N·m, which is between 0.41

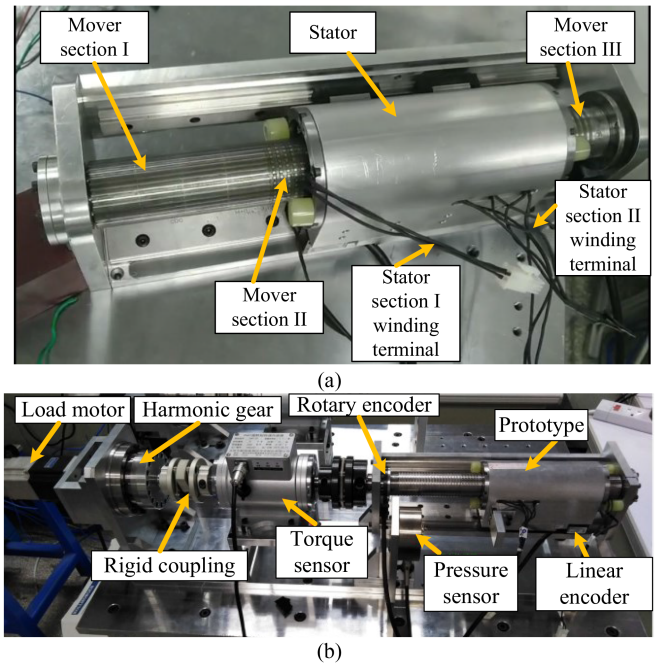

Fig. 16. Prototype and test platform. (a) Prototype. (b) Test bed.

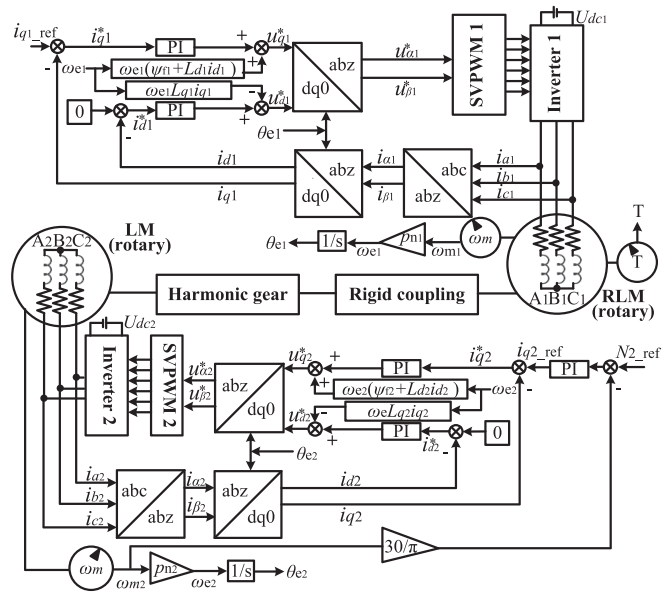

Fig. 17. Control system for the prototype test.

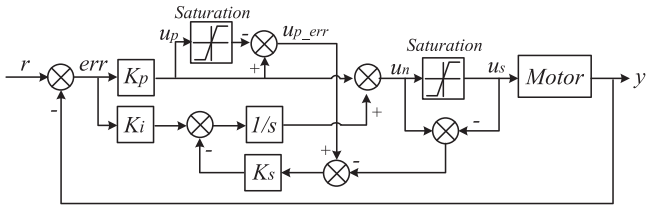

Fig. 18. PI controller with antiwindup.

and 0.06 N·m. From Fig. 15(b), it is clear that the 36th harmonic amplitude has increased by 0.03 N·m, while the 38th and 228th torque harmonics are still almost completely eliminated. It is the same as the predicted result.

V. Performance Test

A. Control Strategy of Test

The prototype of the proposed RLM is shown in Fig. 16(a). It can be seen that there are three different structures in the mover. The two sections of the stator are wrapped in an aluminum shell, and the ends of the two sets of windings are drawn from two positions, respectively. The test platform is shown in Fig. 16(b). For the torque of the mover, the ZH07-20 N·m torque sensor was used for testing. The high-speed load motor is linked to the prototype with a rigid coupling after increasing torque through the harmonic gear. The rotary encoder is used to measure the mover's rotary position. Because the base of the mover is fixed on the test platform, the axial motion is represented by the stator. The force and position of the linear motion are measured with a DYLF-102 pressure sensor and a linear encoder, respectively. It is necessary to use a high-speed motor with a ball screw device as the load during the test.

The control strategy for the torque test is shown in Fig. 17. Here, the prototype uses the current loop control of field-oriented control (FOC) with $i_d = 0$. The speed loop control of the FOC is used on the load motor side. The mover's speed is consistent with the speed of the harmonic gear by rigid coupling. When testing, the armature winding phase current amplitude of the prototype stator Section I is set as i_{q1_ref}. The torque direction of the harmonic gear is opposite to the torque direction of the mover after the stator Section I is powered ON. When the load motor keeps rotating at a constant speed with the stated rotation direction and speed, the load torque is the sum of the RLM output and friction torques. By deducting the average frictional torque at 0 A from the value recorded by the torque sensor, the RLM torque waveform is produced. The force test method is similar to the torque test. It will not be repeated.

B. PI Controller Design

For torque testing, a PI controller is adopted in the current loop. Although differential D is able to reduce the overshoot, in the actual discrete control system, differential is easy to amplify the noise and cause high-frequency vibration oscillation. PI is more convenient for parameter tuning compared to PID. The design of the PI controller with antiwindup, which is applied in the research, is shown in Fig. 18. In the current loop, there are two PI controllers whose inputs are I_d and I_q, respectively [47].

During the actual test, the motor brake is locked, and I_d is assigned a step input of 4 A. In this way, the rated current input can be guaranteed while minimizing the motor motion and suppressing the influence of back EMF on the parametric tuning process. First, K_p is gradually increased until there is no overshoot. Then K_i is adjusted until a steady state error of $\pm 5\%$ can be entered within ten sampling periods. Here, the current sampling period is 0.1 ms.

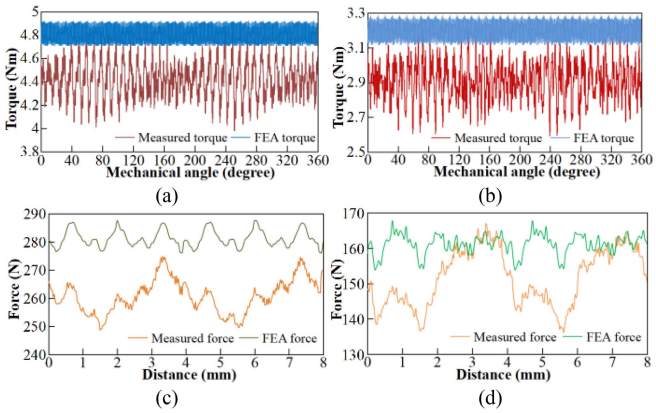

Fig. 19. FEA results and test results. (a) Rotary movement state I. (b) Rotary movement state II. (c) Linear movement state I. (d) Linear movement state II.

Since the motor is rotating at a lower speed during the torque test and the test current range is from 0 A to two times the rated current value, which is 8 A, therefore, the parameters calibrated at 4 A can be used for testing at other currents as well, and the hysteresis and overshoot of the current are inconspicuous. If the stability of the controller is desired to be improved, algorithms such as adaptive fuzzy control can be applied [48].

C. Rated Torque and Force Test

Measured data and simulation data are compared in Fig. 19 under the rated state. The torque data are for a mechanical period, and the force data are for two pole-pair pitches after the current is stabilized. The rated load current is 4 A. The average torques of the two rotating movement states are 4.42 and 2.91 N·m. The average forces of the two linear movement states are 263.73 and 149.49 N. The measured torque and force average values are lower than the simulated values. In Fig. 19, the measured torque and force fluctuations are much larger than the FEA values. The pk2pk values of torque and force are 0.85 N·m, 0.61 N·m, 26.12 N, and 30.79 N. The ripple factor is defined as [49]

$$\begin{cases} \text{ripple factor} = \dfrac{T_{\max}-T_{\min}}{T_{\max}+T_{\min}} \times 100\% \\ \text{ripple factor} = \dfrac{F_{\max}-F_{\min}}{F_{\max}+F_{\min}} \times 100\% \end{cases} \tag{21}$$

where $T_{\max}$, $F_{\max}$, $T_{\min}$, and $F_{\min}$ are the maximum and minimum values in the torque and force waveforms. In the data of FEA, the ripple factors corresponding to the four states of RLM are 2.08%, 2.66%, 2.69%, and 4.31%. In the test, the ripple factors of RLM are 9.62%, 10.48%, 4.95%, and 10.30%. The ripple factors of the measurement are higher than the FEA ripple factor. The FEA and test results are given in Table IV. The measured performance of RLM is inferior to the simulation results as predicted.

D. Experimental Verification of HI

The rated load current I_m is 4 A for four states. The pole-pair numbers p_{rn} and p_{ln} of the RLM are 38 and 2, respectively, in rotary and linear directions. Fig. 19 displays the measurement results for the four states at the rated current. FFT is used to analyze the ripples of rotary movement state I [see Fig. 19(a)] and linear movement state I [see Fig. 19(c)] in the measured data. The results obtained by removing the average component of them are shown in Fig. 20 and Table V. The information on the five harmonic components with the highest amplitude in Fig. 20 is also summarized in Table V. These components are mainly concentrated in the low-frequency band region. The fluctuation at the 36th, 38th, and 228th frequencies is the most prominent in Fig. 20(a). These three frequency fluctuations are also evident in the simulation data with dimension tolerance. Table V also lists the magnitudes and phase angles of the required harmonic

TABLE IV
TORQUE AND FORCE DATA OF RLM

Case	Current	Torque (Force)	Pk2pk	Ripple factor
Rotary movement state I (FEA)	4A	4.80Nm	0.20Nm	2.13%
Rotary movement state II (FEA)	4A	3.20Nm	0.17Nm	2.58%
Linear movement state I (FEA)	4A	283.58N	15.23N	2.04%
Linear movement state II (FEA)	4A	162.49N	14.02N	4.32%
Rotary movement state I (test)	4A	4.42Nm	0.85Nm	9.62%
Rotary movement state II (test)	4A	2.91Nm	0.61Nm	10.48%
Linear movement state I (test)	4A	263.73N	26.12N	4.95%
Linear movement state II (test)	4A	149.49N	30.79N	10.30%

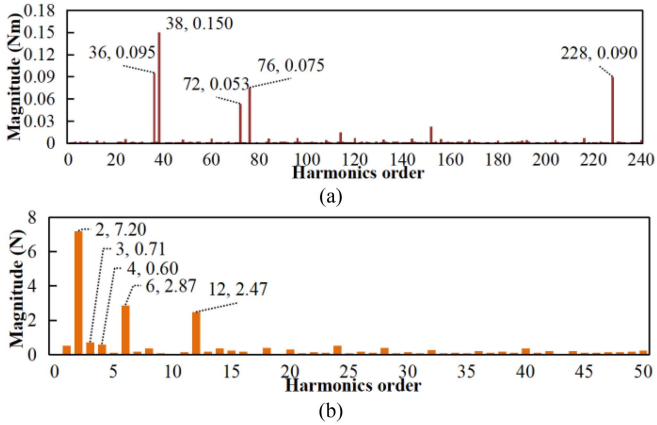

Fig. 20. FFT results of torque and force test data. (a) Rotary movement state I. (b) Linear movement state I.

TABLE V
TORQUE AND FORCE DATA FFT RESULTS AND CURRENT DATA OF HI

Case	k	T_k(Nm)/F_k(N)	φ_k(°)	I_{mk}(A)	n_{ik}	φ_{ik}(°)
Rotary movement state I	38	0.150	272.59	0.136	76	182.59
	36	0.095	71.78	0.086	74	341.78
	228	0.090	333.13	0.082	266	243.13
	76	0.075	103.14	0.068	114	13.14
	72	0.053	10.71	0.048	110	280.71
Linear movement state I	2	7.20	52.49	0.109	4	322.49
	6	2.87	166.05	0.044	8	76.05
	12	2.47	2.23	0.037	14	272.23
	3	0.71	254.96	0.011	5	164.96
	4	0.60	157.17	0.009	6	67.17

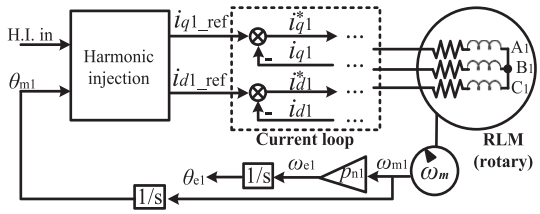

Fig. 21. Control strategy with HI.

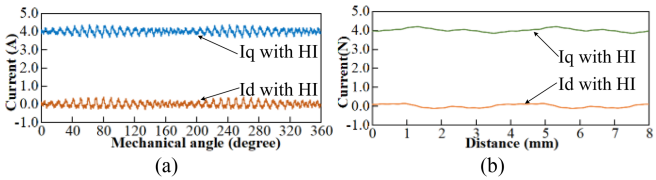

Fig. 22. FEA results and results of test with HI comparison. (a) Rotary movement state I. (b) Linear movement state I.

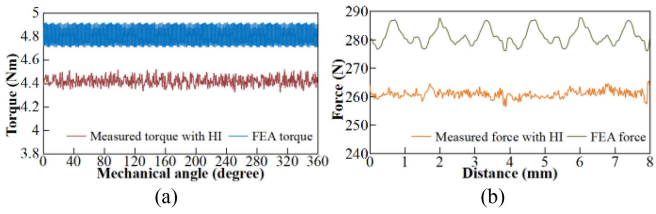

Fig. 23. FEA results and results of test with HI comparison. (a) Rotary movement state I. (b) Linear movement state I.

TABLE VI
TORQUE AND FORCE DATA WITH RIPPLE REDUCTION BY HI

Case	Current	Torque (Force)	Pk2pk	Ripple factor	Ripple reduction
Rotary movement state I (with HI)	4A	4.42Nm	0.19Nm	2.19%	77.23%
Linear movement state I (with HI)	4A	263.73N	8.99N	1.72%	65.25%

current to reduce the torque and force ripples. The fundamental phase angle φ_{upn} of no-load excitation EMF is 90° after zero position calibration.

The harmonic current results calculated by HI are applied to the prototype control system. The whole control system after adding HI is shown in Fig. 21. HI is placed before the current loop. The PI controller used here is the same as in the original test and does not have torque and force ripple suppression features. For the rated state test, add the harmonic current into the control circuit according to Table V. The current waveform for I_d and I_q is in Fig. 22. Here, I_d is not equal to zero all the time. Both I_d and I_q fluctuate around their own rated values. The torque and force waveforms with ripple reduction are shown in Fig. 23. Torque and force ripples decrease significantly, and both ripples are smaller than the ripples in original simulation. Table VI lists the average value and ripple information. The pk2pk values are 0.19 N·m and 8.99 N. The ripple reduction proportions of the two states were 77.66% and 65.57%, respectively. The average

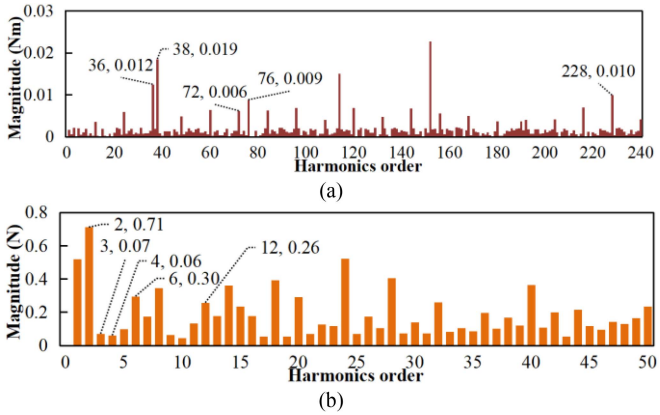

Fig. 24. FFT results of torque and force test data with HI. (a) Rotary movement state I. (b) Linear movement state I.

torque and force have barely changed. FFT analyzed the torque and force waveforms in Fig. 23. The results are in Fig. 24. The marked data are reduced significantly, but the values in Fig. 24(a) are still higher than the simulation results in Fig. 14(b).

This is because there are far more elements with mechanical tolerances in reality than in the simulation. The different harmonics from these tolerances are all superimposed together. Here, only a few harmonic frequencies with higher amplitudes are treated with HI. At the same time, the measurement of torque and position cannot actually be fully synchronized. The harmonic current input will also have a small delay time. In addition, the magnetic saturation degree of the nonlinear material will change when the motor is operated at the rated current in both simulation and experiment. It will distort the waveform of the excited EMF. If φ_{upn} is preset at 90°, there will be some deviation. However, Fig. 23 can prove that this method is effective in reducing torque and force ripples even under the influence such as magnetic saturation and other factors.

The above study shows that fluctuations of torque and force introduced by both motor design and mechanical tolerances can be reduced by HI. It reduces the pressure on machining precision management. Therefore, for different motors machined with the same design, it is possible to adjust their performance to a similar state. If the torque and force ripples can be reduced by the control algorithm, it is extremely helpful to improve the control accuracy of direct-drive motors. HI is used as a feedforward of the current loop to improve the effect, whether the requirement is position, speed, or torque in the control. Because the torque and force harmonics are mainly concentrated in the low-frequency band, HI always has no unique requirements for the hardware. It is sufficient to keep the same closed-loop control as ordinary motors. The existing control equipment can fully meet the requirements of HI. By applying this method, although it introduces some harmonic currents, the amplitude of these harmonic currents is quite low. Therefore, the increase in torque and force fluctuations and iron loss is almost negligible. It is important to admit that before applying HI, a test platform needs to be built and tested for multiple currents at multiple operating speeds to obtain information on torque or force in multiple states. However, these measurements will be simplified with methods

such as the prediction of motor performance through artificial intelligence and the analysis of the correlation between harmonic information and mechanical tolerances.

VI. Conclusion

In automation equipment, a direct-drive motor with multiple DoFs can replace the combination of several motors and transmission mechanisms. It will improve the robustness and stability and decrease the maintenance cost of the equipment. In this article, a novel dual-PM flux modulation direct-drive RLM is proposed.

The structure of the RLM with two cylindrical stator stages arranged axially is learned from previous studies, making the magnetic fields in both directions relatively independent in the novel RLM. The dual-PM flux modulation structure is also used to improve the torque and force densities of the motor. At least 47.8% and 148.0% increases in torque and force densities, respectively, compared to other PM RLMs. It is the first time that the three-section structure of the mover has been adopted, which can improve the torque or force in specific motion areas under the same current load. The improvement ratio is more than 50%. The linear stator has a modular form, resulting in lower motor force fluctuations. Based on the above, the proposed RLM adopts a tooth-slot structure with dual-PM, which reduces the volume of permanent magnets by 50% compared to the surface-mounted PM. The research analyzes the influence of mechanical tolerances on the performance of the motor. It is found that the tolerances will increase the fluctuation mainly at certain frequencies, which is reflected in both simulation and measured data. In order to improve the performance of the direct drive within the current loop of the prototype, HI was designed to reduce torque and force ripples. The effectiveness of HI is demonstrated in both simulation and testing. In the simulation, the pk2pk of torque ripple is reduced by 85.4%. The ripple factors in both states are reduced by 77.23% and 65.25% in the experiment, respectively, with almost constant mean torque and mean force. The robustness of HI has also been confirmed through simulation, and there are no additional hardware requirements for HI applications.

References

[1] K. J. Meessen, J. J. H. Paulides, and E. A. Lomonova, "Analysis and design considerations of a 2-DoF rotary-linear actuator," in *Proc. IEEE Int. Electr. Mach. Drives Conf.*, 2011, pp. 336–341.

[2] L. Gobel and W. Hofmann, "Control of a rotation-thrust drive with helical motor," in *Proc. IEEE 23rd Int. Conf. Ind. Electron., Control, Instrum.*, 1997, vol. 3, pp. 1343–1348.

[3] M. Rabiee and J. J. Cathey, "Verification of a field theory analysis applied to a helical motion induction motor," *IEEE Trans. Magn.*, vol. 24, no. 4, pp. 2125–2132, Jul. 1988.

[4] T. Onuki, W. Jeon, and M. Tanabiki, "Induction motor with helical motion by phase control," in *Proc. IEEE Int. Magn. Conf.*, 1997, p. BR, doi: 10.1109/INTMAG.1997.597506.

[5] G. Wu, X. Wang, Q. Ding, and T. Ni, "Design and analysis of a novel axial actively regulated slotless skew winding bearingless motor," in *Proc. IEEE Int. Conf. Mechatronics Automat.*, 2015, pp. 1864–1869.

[6] S. Tanaka, T. Shimono, and Y. Fujimoto, "Optimal design of length factor for cross-coupled 2-DOF motor with Halbach magnet array," in *Proc. Int. Conf. Mechatronics*, 2015, pp. 529–534.

[7] C. S. Cyusa and Y. Fujimoto, "Enactment-based direct-drive test of a novel radial-Gap Helical Rotlin machine," *IEEE Trans. Ind. Appl.*, vol. 54, no. 2, pp. 1273–1282, Mar./Apr. 2018, doi: 10.1109/tia.2017.2766578.

[8] E. A. Mendrela and E. Gierczak, "Double-winding rotary-linear induction motor," *IEEE Trans. Energy Convers.*, vol. EC-2, no. 1, pp. 47–54, Mar. 1987.

[9] K. Kluszczynski and M. Szczygiel, "How to convert a factory-manufactured induction motor into rotary-linear motor? Part 1: Constructional issues," in *Proc. 15th Int. Workshop Res. Educ. Mechatronics*, 2014, pp. 1–6.

[10] L. Chen and W. Hofmann, "Design of one rotary-linear permanent magnet motor with two independently energized three-phase windings," in *Proc. IEEE 7th Int. Conf. Power Electron. Drive Syst.*, 2007, pp. 1372–1376.

[11] L. Xie, J. Si, Y. Hu, H. Feng, and K. Ni, "Characteristics analysis of the motions of the two-degree-of-freedom direct drive induction motor," *IEEE Trans. Ind. Electron.*, vol. 67, no. 2, pp. 931–941, Feb. 2020, doi: 10.1109/tie.2019.2898590.

[12] J. Si, H. Feng, L. Ai, Y. Hu, and W. Cao, "Design and analysis of a 2-DOF split-stator induction motor," *IEEE Trans. Energy Convers.*, vol. 30, no. 3, pp. 1200–1208, Sep. 2015, doi: 10.1109/tec.2015.2418578.

[13] S.-M. Jang, S.-H. Lee, H. W. Cho, and S. K. Cho, "Design and analysis of helical motion permanent magnet motor with cylindrical Halbach array," *IEEE Trans. Magn.*, vol. 39, no. 5, pp. 3007–3009, Sep. 2003.

[14] M. Bertoluzzo et al., "A distributed driving and steering system for electric vehicles using rotary-Linear Motors," in *Proc. Symp. Power Electron. Elect. Drives Automat. Motion*, 2010, pp. 1156–1159.

[15] P. Bolognesi and L. Taponecco, "FEM modeling of a rotary-linear brushless machine," in *Proc. 17th Int. Conf. Elect. Mach.*, 2006, pp. 1–6.

[16] P. Bolognesi, O. Bruno, F. Papini, V. Biagini, and L. Taponecco, "A low complexity rotary-linear motor useable for actuation of active wheels," in *Proc. Int. Symp. Power Electron. Elect. Drives Automat. Motion*, 2010, pp. 331–338.

[17] L. Xu, M. Lin, X. Fu, and N. Li, "Design and analysis of a double-stator linear–Rotary permanent-magnet motor," *IEEE Trans. Appl. Supercond.*, vol. 26, no. 4, Jun. 2016, Art. no. 0600704, doi: 10.1109/tasc.2016.2517018.

[18] L. Xu, X. Zhu, C. Zhang, L. Zhang, and L. Quan, "Power oriented design and optimization of dual stator linear-rotary generator with Halbach PM array for ocean energy conversion," *IEEE Trans. Energy Convers.*, vol. 36, no. 4, pp. 3414–3426, Dec. 2021, doi: 10.1109/tec.2021.3070633.

[19] W. J. Jeon, M. Tanabiki, T. Onuki, and J. Y. Yoo, "Rotary-linear induction motor composed of four primaries with independently energized ring windings," in *Proc. IEEE Ind. Appl. Conf. 32nd IAS Annu. Meeting*, 1997, no. 1, pp. 365–372.

[20] T. Onuki, W. J. Jeon, and M. Tanabiki, "Induction motor with helical motion by phase control," *IEEE Trans. Magn.*, vol. 33, no. 5, pp. 4218–4220, Sep. 1997.

[21] I. Benţia, M. Ruba, and L. Szabó, "On the control of a rotary-linear switched reluctance motor," in *Proc. 5th Int. Symp. Comput. Intell. Intell. Inform.*, 2011, pp. 41–46.

[22] M. Nezamabadi, E. Afjei, and H. Torkaman, "Design and electromagnetic analysis of a new rotary-linear switched reluctance motor in static mode," *Appl. Comput. Electromagn. Soc. J.*, vol. 31, no. 2, pp. 171–179, 2016.

[23] J. F. Pan, N. C. Cheung, and G. Cao, "A rotary-linear switched reluctance motor," in *Proc. 3rd Int. Conf. Power Electron. Syst. Appl.*, 2009, pp. 1–4.

[24] K. Guo, S. Fang, H. Lin, and H. Yang, "A novel linear-rotary-permanent magnet actuator using interlaced poles," in *Proc. IEEE Magn. Conf.*, 2015, pp. 1–1.

[25] K. Guo, S. Fang, H. Lin, H. Yang, Y. Huang, and P. Jin, "3-D analytical analysis of magnetic field of flux reversal linear-rotary permanent-magnet actuator," *IEEE Trans. Magn.*, vol. 53, no. 6, Jun. 2017, Art. no. 8202205.

[26] K. Guo and Y. Guo, "Key parameter design and analysis of flux reversal linear rotary permanent magnet actuator," *IEEE Trans. Appl. Supercond.*, vol. 29, no. 2, Mar. 2019, Art. no. 0600405, doi: 10.1109/tasc.2018.2889625.

[27] K. Guo, S. Fang, H. Yang, H. Lin, and S. L. Ho, "A novel linear-rotary permanent-magnet actuator using interlaced poles," *IEEE Trans. Magn.*, vol. 51, no. 11, Nov. 2015, Art. no. 8207004.

[28] J.-S. Shin, R. Watanabe, T. Koseki, and H.-J. Kim, "Transverse-flux-type cylindrical linear synchronous motor using generic armature cores for rotary machinery," *IEEE Trans. Ind. Electron.*, vol. 61, no. 8, pp. 4346–4355, Aug. 2014, doi: 10.1109/tie.2013.2274426.

[29] S. M. Miric, R. V. Giuffrida, D. Bortis, and J. W. Kolar, "Enhanced complex space vector modeling and control system design of multiphase magnetically levitated rotary–Linear machines," *IEEE J. Emerg. Sel. Topics Power Electron.*, vol. 8, no. 2, pp. 1833–1849, Jun. 2020, doi: 10.1109/jestpe.2019.2945625.
[30] P. Jin, S. Fang, H. Lin, Z. Q. Zhu, Y. Huang, and X. Wang, "Analytical magnetic field analysis and prediction of cogging force and torque of a linear and rotary permanent magnet actuator," *IEEE Trans. Magn.*, vol. 47, no. 10, pp. 3004–3007, Oct. 2011.
[31] P. Jin, H. Lin, S. Fang, and S. Ho, "Decoupling control of linear and rotary permanent magnet actuator using two-directional d-q transformation," *IEEE Trans. Magn.*, vol. 48, no. 10, pp. 2585–2591, Oct. 2012.
[32] T. T. Overboom, J. W. Jansen, E. A. Lomonova, and F. J. F. Tacken, "Design and optimization of a rotary actuator for a two-degree-of-freedom zφ-module," *IEEE Trans. Ind. Appl.*, vol. 46, no. 6, pp. 2401–2409, Nov./Dec. 2010, doi: 10.1109/tia.2010.2073430.
[33] A. Turner, K. Ramsay, R. Clark, and D. Howe, "Direct-drive rotary-linear electromechanical actuation system for control of gearshifts in automated transmissions," in *Proc. IEEE Veh. Power Propul. Conf.*, 2007, pp. 267–272.
[34] Y. Ma and W. N. Fu, "Design and comparison of Vernier permanent-magnet machines with different winding types based on fractional-slot windings," *IEEE Trans. Magn.*, vol. 57, no. 6, Jun. 2021, Art. no. 8105105.
[35] C. Liu, C. H. T. Lee, and M. Chen, "Comparison of outer-rotor permanent magnet machines for in-wheel drives," in *Proc. IEEE Int. Symp. Ind. Electron.*, 2013, pp. 1–6.
[36] D. K. Jang and J. H. Chang, "Design of a Vernier machine with PM on both sides of rotor and stator," *IEEE Trans. Magn.*, vol. 50, no. 2, Feb. 2014, Art. no. 7021704, doi: 10.1109/tmag.2013.2284509.
[37] S. U. Chung, J. W. Kim, B. C. Woo, D. K. Hong, J. Y. Lee, and D. H. Koo, "A novel design of modular three-phase permanent magnet Vernier machine with consequent pole rotor," *IEEE Trans. Magn.*, vol. 47, no. 10, pp. 4215–4218, Oct. 2011.
[38] S. Niu, S. L. Ho, and W. N. Fu, "A novel stator and rotor dual PM Vernier motor with space vector pulse width modulation," *IEEE Trans. Magn.*, vol. 50, no. 2, Feb. 2014, Art. no. 7019904, doi: 10.1109/tmag.2013.2280758.
[39] G. Feng, C. Lai, and N. C. Kar, "A closed-loop fuzzy-logic-based current controller for PMSM torque ripple minimization using the magnitude of speed harmonic as the feedback control signal," *IEEE Trans. Ind. Electron.*, vol. 64, no. 4, pp. 2642–2653, Apr. 2017.
[40] X. Wang, C. Jiang, F. Zhuang, C. H. T. Lee, and C. C. Chan, "A harmonic injection method equivalent to the resonant controller for speed ripple reduction of PMSM," *IEEE Trans. Ind. Electron.*, vol. 69, no. 10, pp. 9793–9803, Oct. 2022.
[41] Z. Wu, Z. Yang, K. Ding, and G. He, "Order-domain-based harmonic injection method for multiple speed harmonics suppression of PMSM," *IEEE Trans. Power Electron.*, vol. 36, no. 4, pp. 4478–4487, Apr. 2021.
[42] W. Huang, W. Hua, X. Zhu, Y. Fan, and M. Cheng, "Comparison of cogging torque compensation methods for a flux-switching permanent magnet motor by harmonic current injection and iterative learning control," in *Proc. Int. Conf. Elect. Mach.*, 2020, pp. 1971–1977.
[43] M. A. Amirian, A. Rashidi, and S. M. S. Nejad, "Torque ripple reduction of permanent magnet synchronous motor with non-sinusoidal back EMF using a modified and simplified current optimization technique," in *Proc. 6th Power Electron., Drive Syst. Technol. Conf.*, 2015, pp. 322–327.
[44] I. Boldea and S. A. Nasar, *Linear Electric Actuators and Generators*. Cambridge, U.K.: Cambridge Univ. Press, 1997.
[45] Q. Lin, S. Niu, F. Cai, W. Fu, and L. Shang, "Design and optimization of a novel dual-PM machine for electric vehicle applications," *IEEE Trans. Veh. Technol.*, vol. 69, no. 12, pp. 14391–14400, Dec. 2020, doi: 10.1109/tvt.2020.3034573.
[46] P. Jin, Y. Yuan, G. Jian, H. Lin, S. Fang, and H. Yang, "Static characteristics of novel air-cored linear and rotary Halbach permanent magnet actuator," *IEEE Trans. Magn.*, vol. 50, no. 2, Feb. 2014, Art. no. 7024204, doi: 10.1109/tmag.2013.2284277.
[47] L. Wang, *PID Control System Design and Automatic Tuning Using MATLAB/Simulink*. Hoboken, NJ, USA: Wiley, 2020.
[48] L. Harnefors and H.-P. Nee, "Model-based current control of AC machines using the internal model control method," *IEEE Trans. Ind. Appl.*, vol. 34, no. 1, pp. 133–141, Jan./Feb. 1998, doi: 10.1109/28.658735.
[49] P. Fernández, J. A. Güemes, and A. Iraolagoitia, "Influence of flux estimation in performance of direct torque control of PMSM," *Renewable Energy Power Qual. J.*, vol. 1, pp. 1184–1189, 2013, doi: 10.24084/repqj11.572.

Yue Ma received the B.E. degree in electrical and electronic engineering from the Harbin University of Science and Technology, Harbin, China, in 2014, and the M.Sc. degree in electrical engineering in 2016 from The Hong Kong Polytechnic University, Kowloon, Hong Kong, where she is currently working toward the Ph.D. degree in electrical engineering.

Her main research interests include design, analysis, optimization and control of electric machines for automation equipment.

Shuangxia Niu (Senior Member, IEEE) received the B.Sc. and M.Sc. degrees in electrical engineering from the School of Electrical Engineering and Automation, Tianjin University, Tianjin, China, in 2002 and 2005, respectively, and the Ph.D. degree in electrical engineering from the Department of Electrical and Electronic Engineering, The University of Hong Kong, Hong Kong, in 2009.

Since 2009, she has been with The Hong Kong Polytechnic University, Kowloon, Hong Kong, where she is currently an Associate Professor with the Department of Electrical Engineering. She has authored or coauthored more than 100 articles in leading journals. Her research interests include novel electrical machines and drives, renewable energy conversion systems, and applied electromagnetics.

Weinong Fu received the B.Eng. degree in electrical engineering from the Hefei University of Technology, Hefei, China, in 1982, the M.Eng. degree in electrical engineering from the Shanghai University of Technology, Shanghai, China, in 1989, and the Ph.D. degree in electrical engineering from The Hong Kong Polytechnic University, Kowloon, Hong Kong, in 1999.

He is currently a Professor with the Shenzhen Institutes of Advanced Technology, Chinese Academy of Sciences, Beijing, China. For 13 years, he was an Associate Professor and a Full Professor with PolyU. He was a Key Developer with Ansoft Corporation, Pittsburgh, PA, USA. He has about seven years of working experience with Ansoft, focusing on the development of commercial software Maxwell. He has made many contributions to the theory and application of electromagnetic field computation and electric device designs, including the publication of more than 250 refereed journal papers. His research interests include computational electromagnetics, optimal design of electric devices, applied electromagnetics, and novel electric machines.

Jiaqi Fei received the B.E. degree in mechanical engineering from the Nanjing University of Science and Technology, Nanjing, China, and the M.S. degree in mechanical and aerospace engineering from George Washington University, Washington, DC, USA, in 2014 and 2016, respectively, with a focus in control theories in mechanical and electronic systems.

He is currently with Han's Robot Corporation, Shenzhen, China, where his research is focused on high-performance motor control for robotic applications. His interests include robot arms, control systems, motor drives, embedded systems, and automation technologies.